The Astrophysical Journal, 898:59 (10pp), 2020 July 20 https://doi.org/10.3847/1538-4357/ab9a44

Intrinsic Properties of the Engine and Jet that Powered the Short Gamma-Ray Burst Associated with GW170817

Davide Lazzati[1], Riccardo Ciolfi[2,3], and Rosalba Perna[4,5]
[1] Department of Physics, Oregon State University, 301 Weniger Hall, Corvallis, OR 97331, USA
[2] INAF, Osservatorio Astronomico di Padova, Vicolo dell'Osservatorio 5, I-35122 Padova, Italy
[3] INFN, Sezione di Padova, Via Francesco Marzolo 8, I-35131 Padova, Italy
[4] Department of Physics and Astronomy, Stony Brook University, Stony Brook, NY 11794-3800, USA
[5] Center for Computational Astrophysics, Flatiron Institute, New York, NY 10010, USA
Received 2020 April 21; revised 2020 June 1; accepted 2020 June 5; published 2020 July 23

Abstract

GRB 170817A was a subluminous short gamma-ray burst detected about 1.74 s after the gravitational wave signal GW170817 from a binary neutron star (BNS) merger. It is now understood as an off-axis event powered by the cocoon of a relativistic jet pointing 15°–30° away from the direction of observation. The cocoon was energized by the interaction of the incipient jet with the non-relativistic baryon wind from the merger remnant, resulting in a structured outflow with a narrow core and broad wings. In this paper, we couple the observational constraints on the structured outflow with a model for the jet–wind interaction to constrain the *intrinsic* properties with which the jet was launched by the central engine, including its time delay from the merger event. Using wind prescriptions inspired by magnetized BNS merger simulations, we find that the jet was launched within about 0.4 s from the merger, implying that the 1.74 s observed delay was dominated by the fireball propagation up to the photospheric radius. We also constrain, for the first time for any gamma-ray burst, the jet opening angle at injection and set a lower limit to its asymptotic Lorentz factor. These findings suggest an initially Poynting-flux dominated jet, launched via electromagnetic processes. If the jet was powered by an accreting black hole, they also provide a significant constraint on the survival time of the metastable neutron star remnant.

Unified Astronomy Thesaurus concepts: Gamma-ray bursts (629); Gravitational wave sources (677); Stellar mergers (2157)

1. Introduction

The discovery of the gravitational wave (GW) source GW170817 (Abbott et al. 2017a) marked the first detection of GWs from a binary neutron star (BNS) merger. The observation of the same source in the electromagnetic spectrum, from the almost simultaneous γ-rays (Abbott et al. 2017b; Goldstein et al. 2017; Savchenko et al. 2017) to the later X-ray and UV, optical, IR, and radio signals (Abbott et al. 2017c), allowed, among other astrophysical implications, to firmly establish the connection between short gamma-ray bursts (SGRBs) and BNS mergers (e.g., Abbott et al. 2017b; Goldstein et al. 2017; Hallinan et al. 2017; Kasliwal et al. 2017; Savchenko et al. 2017; Troja et al. 2017; Lazzati et al. 2018; Mooley et al. 2018; Ghirlanda et al. 2019).

The early UV, optical, and IR radiation, detected within about a day from the GW/γ-ray detection, were shown to be consistent, both spectrally and temporally, with the expectations of a kilonova (e.g., Arcavi et al. 2017; Soares-Santos et al. 2017; Pian et al. 2017), i.e., a transient powered by the radioactive decay of heavy r-process elements synthesized within the matter ejected during and after merger. The later X-ray (Troja et al. 2017) and radio emission (Hallinan et al. 2017), first detected $\gtrsim$10 days after the trigger, followed a single power-law spectrum over more than eight orders of magnitude in energy (Lyman et al. 2018). This suggested an origin in a blastwave, and the spectral-temporal characteristics of the observed radiation were used to constrain the properties of the emission region. An isotropic fireball, as well as a top-hat jet (i.e., a jet with sharp edges) were ruled out early on (Kasliwal et al. 2017). However, it was only with Very Large Array observations that the presence of a relativistic collimated jet—suggested by early modeling (Lazzati et al. 2018; Ioka & Nakamura 2018) and by the steep radio decay (Lamb et al. 2018, 2019)—was confirmed beyond doubt (Mooley et al. 2018; Ghirlanda et al. 2019), hence establishing the consistency with a standard, cosmological SGRB observed off-axis.

The production of jets by astrophysical sources, which is an essential ingredient for both long and short GRBs, is an area of much interest in astrophysics. In order to understand the mechanisms by which jets are produced and launched, the first step is the characterization of their *intrinsic* properties, i.e., the jets' properties as released by their central engines, before any interaction with the surrounding material. However, what we observe are the properties of the outflow when it becomes transparent to radiation, molded by the environment in which it has propagated. In the case of long GRBs this environment is the envelope of a massive star (MacFadyen et al. 2001), while in the case of SGRBs it is the material expelled in a compact binary merger (e.g., Rosswog et al. 1999; Fernández & Metzger 2013; Ciolfi et al. 2017; Radice et al. 2018; Ciolfi et al. 2019).

A model able to compute the SGRB outflow properties resulting from the jet interaction with the surrounding material was recently developed by Lazzati & Perna (2019), employing a semi-analytical method calibrated via numerical simulations (see also Salafia et al. 2020). Such a model takes as input the properties of the surrounding material (most importantly its

Table 1
Physical Quantities and Ranges of Prior Distributions for the Input Parameters

Symbol	Range	Units	Explanation
$E_{\rm j}$	5×10^{48}–2×10^{50}	erg	Total jet energy
$T_{\rm eng}$	0.1–2.0	s	Duration of the engine activity
$L_{\rm j}$	derived	erg s^{-1}	Jet luminosity (constant over the engine activity)
η	10–3000	⋯	Asymptotic Lorentz factor of the jet
$\theta_{\rm j}$	1–45	deg	Initial jet half-opening angle at injection
$\Delta t_{\rm m-j}$	0–1.75	s	Time delay between merger and jet launching time
$\theta_{\rm l.o.s.}$	1–45	deg	Viewing angle with respect to the jet axis

mass and velocity), those of the jet (namely its asymptotic Lorentz factor, injection angle, and time delay between the merger and the jet launching), and the viewing angle, i.e., the angle between the jet axis and the line of sight. Here, we apply this model to constrain the injection parameters of the jet from GW170817. For the properties of the surrounding material, we refer to the results of general relativistic magnetohydrodynamics (GRMHD) simulations of BNS mergers performed by Ciolfi et al. (2017). We also consider a more general parametric description as an alternative. For the jet intrinsic properties, we explore a conservative range for all the relevant parameters.

Constraints for the time interval between merger and jet launching have been discussed before in the literature, with somewhat controversial results. Studies based on the need to eject enough material to support a kilonova (Gill et al. 2019) and structure in the jet (Granot et al. 2017) favor a long merger–jet delay of the order of one second. Such a delay, however, requires a coincidence with the propagation time of the jet to yield a total observed delay of ∼1.74 s. This, and the fact that the pulse duration of GRB170817A coincides with the total observed delay favors instead a much shorter merger–jet delay (Lin et al. 2018; Zhang et al. 2018; Zhang 2019). Short time delays have also been suggested by population synthesis calculations of SGRBs (Belczynski et al. 2006; Beniamini et al. 2020a).

Our paper is organized as follows: Section 2 describes the employed methods, based on the model developed by Lazzati & Perna (2019), as well as the range of values allowed for the input parameters (for the jet and the surrounding material) and the observational constraints from GW170817/GRB 170817A that we enforce. The results of our study are presented in Section 3. Then, we summarize and discuss our results in Section 4.

2. Methods

Our reference scenario is a BNS merger forming a (meta)stable massive neutron star (NS) remnant that might eventually collapse to a black hole (BH). We assume that a SGRB jet is launched at a time $\Delta t_{\rm m-j}$ after merger, either by the massive NS or right after BH formation (see, e.g., Ciolfi 2018). In both cases, a nearly isotropic baryon-loaded wind from the NS remnant continuously pollutes the surrounding environment for a time $\Delta t_{\rm m-j}$ before the jet is launched. Our model describes the propagation of the incipient jet across such an environment and the resulting properties and structure of the final escaping outflow.[6] Throughout the manuscript, we will refer to the incipient collimated outflow from the central engine with high-entropy (and eventually high-Lorentz factor) as "jet," to the wide-angle non-relativistic matter released by the massive NS remnant prior to jet launching as "wind," and to the ultimate structured outflow at large distances resulting from the jet–wind interaction as "outflow."

The analysis that we present is based on the jet–wind interaction model developed by Lazzati & Perna (2019). By imposing energy conservation and pressure balance at the jet, cocoon and wind interfaces (Begelman & Cioffi 1989; Matzner 2003; Lazzati & Begelman 2005; Morsony et al. 2007; Bromberg et al. 2011), they were able to develop a set of semi-analytic equations to compute the properties of the outflow for any given jet and wind setup. The underlying assumptions are the following: (i) the jet has initially a top-hat structure, with uniform properties within a half-opening angle $\theta_{\rm j}$; (ii) the engine turns on at time $\Delta t_{\rm m-j}$ after merger, releasing a constant luminosity $L_{\rm j}$ for a time $T_{\rm eng}$ and then turning off; and (iii) the jet is characterized by a constant dimensionless entropy η, which corresponds to the maximum asymptotic Lorentz factor that the jet material would attain if the acceleration were complete and dissipationless.

For the wind, we consider two different prescriptions. In the first, we model the wind following the results of GRMHD simulations of BNS mergers by Ciolfi et al. (2017). In particular, we refer to the outcome of their simulations for two possible equations of state (EOS), APR4 (Akmal et al. 1998) and H4 (Glendenning & Moszkowski 1991), and for two values of the mass ratio, $q=1$ and $q=0.9$,[7] labeled as q10 and q09, respectively. For these different cases, we impose an isotropic wind with a constant mass-flow rate matching the value given in Figure 23 of Ciolfi et al. (2017) and constant velocity equal to the reported escape velocity, namely $v_{\rm w}=0.11\,c$, $0.12\,c$, $0.13\,c$, and $0.11\,c$ for the APR4q09, APR4q10, H4q09, and H4q10 models, respectively. In our second prescription, the wind is instead parametrized and we consider constant mass-flow rate and velocity spanning a wide range of values, namely $0.001\leqslant \dot{m}_{\rm w}/(M_\odot\ {\rm s}^{-1})\leqslant 1$ and $0.05\leqslant v_{\rm w}/c\leqslant 0.25$. In all cases, the wind starts at the time of merger and persists at least until the engine turns off.

Our analysis proceeds as follows. A random set of parameter values is first generated for the system. These are the jet entropy η, total emitted energy $E_{\rm j}$, half-opening angle $\theta_{\rm j}$, duration of the engine activity $T_{\rm eng}$, delay time of the jet launching $\Delta t_{\rm m-j}$, and viewing angle with respect to the jet axis $\theta_{\rm l.o.s.}$ (see Table 1). For the parametrized wind case, the list includes also the mass-flow rate $\dot{m}_{\rm w}$ and the wind velocity $v_{\rm w}$. All these parameters are randomly drawn from flat prior

[6] We note that we are not considering dynamical (tidal and shock-driven) ejecta from the merger process itself as a potential obstacle for the jet propagation as these are mostly expelled at high latitude (i.e., away from the jet axis). Moreover, this matter is ejected only within ∼10 ms from the merger time and at larger speed, thus already far away by the time the jet is launched.

[7] The BNS total mass in the simulations is fixed and differs by only ≈1% from the one inferred for GW170817.

Table 2
Observational Constraints on Derived Physical Quantities

Symbol	Range	Units	Description
$E_{\rm iso,l.o.s.}$	3×10^{47}–2×10^{50}	erg	The outflow isotropic-equivalent energy along the line of sight
$\Gamma_{\rm l.o.s.}$	1.5–10	⋯	The Lorentz factor of the outflow along the line of sight
$\theta_{\rm core}$	1.5–4	deg	The half-opening angle of the core of the outflow
$\Delta t_{\rm obs}$	1.5–1.75	s	The observed delay between merger time and prompt gamma-ray pulse

distributions within a range that is either theoretically reasonable or constrained by observations. We assumed the following priors for the injection properties:

1. The jet is launched with an asymptotic Lorentz factor $10 \leqslant \eta = L_{\rm j}/\dot{m}c^2 \leqslant 3000$. The conservative lower limit is set by observational constraints (e.g., Ghirlanda et al. 2019), while the upper limit is simply set to a rather large value.
2. The jet total energy is limited to $5\times10^{48} \leqslant E_{\rm j}/{\rm erg} \leqslant 2\times10^{50}$. These values are conservative compared to the observational constraints (e.g., Fong et al. 2015).
3. The initial half-opening angle of the jet is limited to $1^\circ \leqslant \theta_{\rm j} \leqslant 45^\circ$. In this case we strove to consider a range as large as possible. The lower limit of 1 degree is set to avoid a divergence at 0, while the upper limit of 45° is conservatively larger than any successful jet that has been numerically studied (Murguia-Berthier et al. 2014, 2017; Nagakura et al. 2014; Lazzati et al. 2017b; Nakar et al. 2018; Xie et al. 2018; Hamidani et al. 2020; Lyutikov 2020).
4. The delay time between the BNS merger and the jet launching is limited to $0 \leqslant \Delta t_{\rm m-j} \leqslant 1.75$ s. The upper limit in this case is set by the observed time delay (Abbott et al. 2017b).
5. The viewing angle is limited to $1^\circ \leqslant \theta_{\rm l.o.s.} \leqslant 45^\circ$. As for the injection angle, the lower limit is set to avoid a divergence at 0, while the upper limit is larger than the one obtained from both GWs and electromagnetic observations (Abbott et al. 2017b; Mooley et al. 2018; Ghirlanda et al. 2019).
6. The duration of the engine activity is limited to $0.1\ {\rm s} \leqslant T_{\rm eng} \leqslant 2$ s. In this case the lower limit is set to avoid a divergence at 0, while the upper limit is chosen to be at the traditional separation between long and short GRBs (Kouveliotou et al. 1993).

Once the jet and wind parameters have been drawn, the code computes the properties of the outflow.[8] The procedure is repeated for over 100 million random samples. The resulting outflow properties are then checked against further observational constraints and only consistent models are retained. The additional constraints that we enforce are the following (see also Table 2):

1. The isotropic-equivalent energy of the outflow in the direction of the line of sight has to be within the range $3\times10^{47} \leqslant E_{\rm iso,l.o.s.}/{\rm erg} \leqslant 2\times10^{50}$. The lower limit is set by assuming an efficiency of 10% for the prompt gamma-ray emission (Abbott et al. 2017b). The upper limit is obtained by analyzing various best-fit models from the literature (Alexander et al. 2018; D'Avanzo et al. 2018; Lazzati et al. 2018; Nakar & Piran 2018; Mooley et al. 2018; Wu & MacFadyen 2018; Ghirlanda et al. 2019; Hotokezaka et al. 2019).
2. The half-opening angle of the core of the outflow (or final escaping jet) is limited to $1.^\circ3 \leqslant \theta_{\rm core} \leqslant 4^\circ$. This constraint comes exclusively from the modeling of proper motion and spatial extent of the radio counterpart (Mooley et al. 2018; Ghirlanda et al. 2019). Note that both Mooley et al. (2018) and Ghirlanda et al. (2019) use power-law outflow models, while here we use a double exponential profile. To compensate for such difference, we re-scaled by a factor of 1.75 the opening angle values suggested by their analyses. As shown in Figure 1, this compensation provides a rather good match between our angular profiles and theirs.
3. The observed time delay between the merger (or the peak of the GW signal) and the gamma-ray detection is constrained to be $1.5\ {\rm s} \leqslant \Delta t_{\rm obs} \leqslant 1.75$ s and is given by the sum of three terms (Zhang 2019):

$$\Delta t_{\rm obs} = \Delta t_{\rm m-j} + \frac{R_{\rm bo}}{c}\frac{1-\beta_{\rm jh}}{\beta_{\rm jh}} + \frac{R_{\rm ph,l.o.s.}-R_{\rm bo}}{c}\frac{1-\beta_{\rm l.o.s.}}{\beta_{\rm l.o.s.}}, \quad (1)$$

where $R_{\rm bo}$ is the radius at which the jet breaks out of the wind, $\beta_{\rm jh}$ is the speed of the head of the jet inside the wind in units of c, $R_{\rm ph,l.o.s.}$ is the photospheric radius of

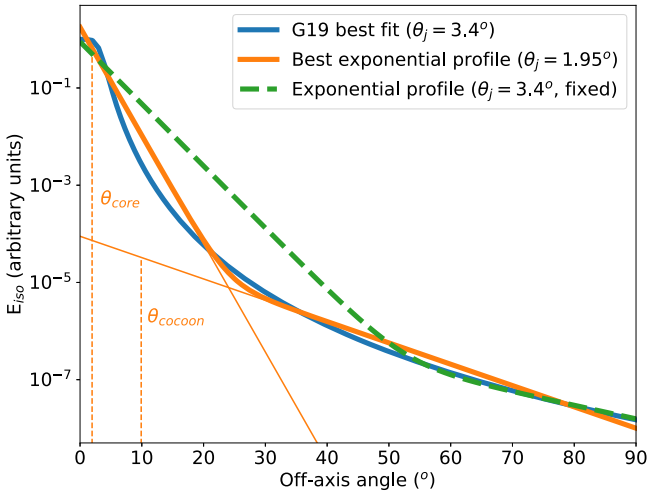

Figure 1. Comparison between the best-fit outflow structure from Ghirlanda et al. (2019, G19 in the legend) and the exponential profile used in this work. It is found that a scaling factor of 1.75 between the core opening angles is necessary for a good match of the angular the profiles. Also shown with a dashed green line is the exponential profile for a core angle equal to the G19 best-fit value. Vertical dashed orange lines show the values of $\theta_{\rm core}$ and $\theta_{\rm cocoon}$ for the exponential outflow profile.

[8] The jet is launched from a nozzle at $r_0 = 10^7$ cm with an initial Lorentz factor of $\Gamma = 1$.

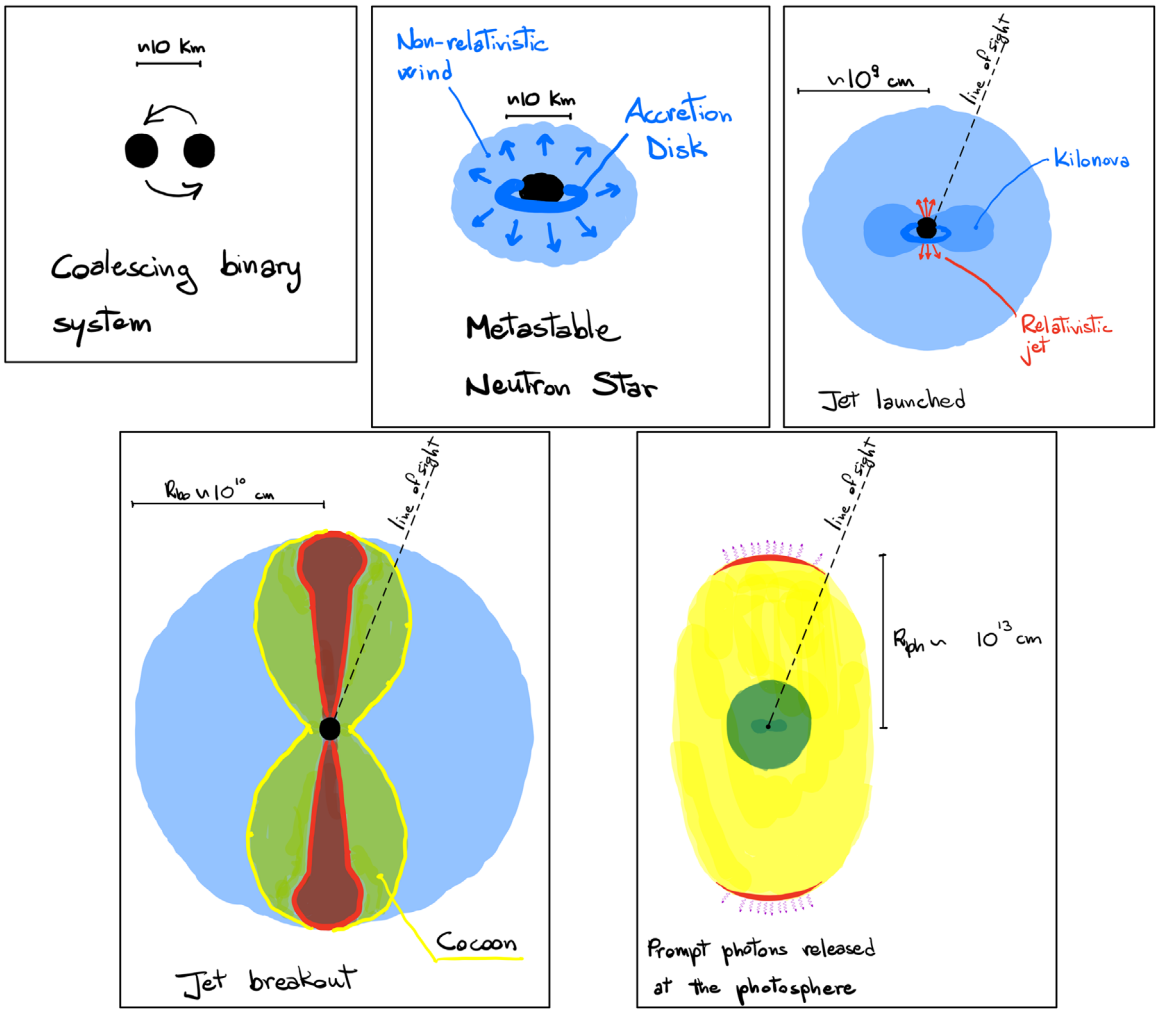

Figure 2. Cartoon of the various phases of the merger/outflow phenomenology, indicating the relevant radii. Numerical values are order-of-magnitude estimates, the actual values changing for each simulation.

the outflow, and $\beta_{\rm l.o.s.}$ is its velocity in units of c, both measured along the line of sight of the observation. Figure 2 shows the location of the various radii throughout the evolution of the merger and subsequent outflow. Here we have considered a fairly wide interval, down to 1.5 s, to take into account the fact that the beginning of the gamma-ray emission may have been misidentified if initially below the the background.

4. The initial Lorentz factor of the material moving along the line of sight is within the interval $1 \leqslant \Gamma_{\rm l.o.s.} \leqslant 10$. This is a conservative constraint obtained from combining various afterglow models (Alexander et al. 2018; D'Avanzo et al. 2018; Lazzati et al. 2018; Mooley et al. 2018; Wu & MacFadyen 2018; Ghirlanda et al. 2019; Hotokezaka et al. 2019; Beniamini et al. 2020b).

2.1. Calculation of the Photospheric Radius

A critical piece of information for constraining the observed time delay is the calculation of the location of the photosphere (see Equation (1)). Calculations of the photospheric radius in gamma-ray burst outflows have been commonly performed either in the approximation of a thin shell or of an infinite wind (e.g., Mészáros & Rees 2000; Daigne & Mochkovitch 2002). A large Lorentz factor for which $(1-\beta) \simeq 1/2\Gamma^2$ has also been assumed. In the case of off-axis outflows, all approximations should be relaxed, since relatively slow outflows in thick—but not infinite—shells are relevant. In addition, it has been customary to assume a neutron free fireball in past GRB literature, for which $Y_{\rm e} \equiv \frac{n_{\rm p}}{n_{\rm p}+n_{\rm n}} = 1$. Here, $n_{\rm p}$ and $n_{\rm n}$ are the proton and neutron densities, respectively, and we generalize the equations for the photospheric radius to the case of an outflow with $Y_{\rm e} \leqslant 1$. We assume our fiducial electron fraction to be $Y_{\rm e} = 0.5$ or lower, as expected for most GRB engines (Beloborodov 2003), but quote also results for $Y_{\rm e} = 1$.

Let us consider a photon that is at the back of the outflow. If its location corresponds to the photospheric radius, then the photon has probability $1/2$ of undergoing a scattering before leaving the flow at the front. We can therefore write a condition on the opacity such that

$$\tau = \frac{2}{3} = \int_{R_{\rm ph}}^{R_{\rm ph}+\Delta} n_{\rm e}\sigma_T(1-\beta\cos(\theta_{\gamma e}))\,dr, \qquad (2)$$

where $R_{\rm ph}+\Delta$ is the outer radius of the outflow at the time at which the photon leaves the outflow, $n_{\rm e}$ is the fireball's electron number density in the observer frame, and $\theta_{\gamma}e$ is the angle between the photon's and the outflow's velocity vectors.

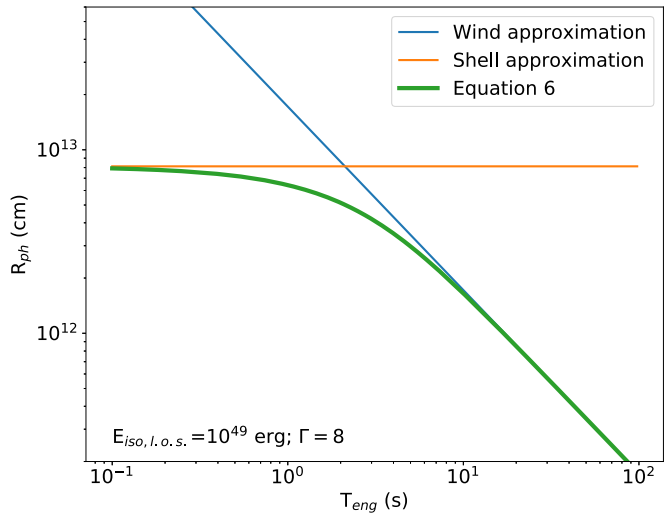

Figure 3. Comparison between the solution for the photospheric radius given in Equation (6) and the approximations for an infinite wind and a thin shell.

Assuming $\theta_\gamma e \sim 1/\Gamma$, we have

$$\frac{2}{3} = \frac{L_{\rm iso,\,l.o.s.} Y_{\rm e} \sigma_T (1-\beta)}{4\pi m_p c^3 \eta} \int_{R_{\rm ph}}^{R_{\rm ph}+\frac{cT_{\rm eng}}{1-\beta}} \frac{dr}{r^2}, \quad (3)$$

where $\sigma_{\rm T}$ is the Thomson cross section, and we have used

$$n_{\rm e} = \frac{L_{\rm iso,l.o.s.} Y_{\rm e}}{4\pi r^2 m_{\rm p} c^3 \eta}. \quad (4)$$

We have also assumed that the fireball is fully accelerated by the time it reaches the photospheric radius, which is reasonable for a low Lorentz factor outflow. Here we have used the subscript $_{\rm l.o.s.}$ to remind the reader that the calculated photospheric radius is for material moving along the line of sight to the observer.

Performing a trivial integration we obtain

$$\frac{2}{3} = \frac{L_{\rm iso,l.o.s.} Y_{\rm e} \sigma_T (1-\beta)}{4\pi m_p c^3 \eta} \left(\frac{1}{R_{\rm ph}} - \frac{1}{R_{\rm ph} + \frac{cT_{\rm eng}}{1-\beta}} \right), \quad (5)$$

which is solved to yield

$$R_{\rm ph} = \frac{\sqrt{\left(\frac{cT_{\rm eng}}{1-\beta}\right)^2 + \frac{3}{2\pi}\frac{L_{\rm iso,l.o.s.} Y_{\rm e} \sigma_T T_{\rm eng}}{m_p c^2 \eta}} - \frac{cT_{\rm eng}}{1-\beta}}{2}. \quad (6)$$

Note that the latter equation is valid for any shell thickness, and that it has the correct asymptotic behavior for a high-Lorentz factor wind case, for which $(1-\beta) = 1/2\eta^2$:

$$\lim_{T_{\rm eng}\to\infty;\eta\to\infty} R_{\rm ph} = \frac{3}{16\pi} \frac{L_{\rm iso,l.o.s.} Y_{\rm e} \sigma_T}{\eta^3 m_p c^3}. \quad (7)$$

In the opposite extreme of a thin fireball, we obtain[9]

$$\lim_{T_{\rm eng}\to 0;\eta\to\infty} R_{\rm ph} = \sqrt{\frac{3E_{\rm iso,l.o.s.} Y_{\rm e} \sigma_T}{2\pi\eta m_p c^2}}. \quad (8)$$

[9] In this case we note that the result differs by a factor η from the equation that was previously derived, e.g., in Lazzati et al. (2017a) since that derivation did not consider the expansion of the outer edge of the fireball while the photon crosses it.

Figure 3 shows, for an outflow with properties similar to those revealed by GRB 170817A along the line of sight, how the result of Equation (6) depends on the engine duration $T_{\rm eng}$. Also shown are the two limiting cases of wind and shell approximations, correctly recovered. In all the calculations of this paper, we use the more general Equation (6).

3. Results

The results of the analysis are best shown through corner plots, where each of the model parameters is plotted versus the other ones. In the corner plot figures, the colored panels show the density map of models that satisfy the observational constraints, while the solid lines mark the areas of 1σ, 2σ, and 3σ statistical significance level. Histograms on the diagonal show the posterior probability distribution for each parameter marginalized over the others. Finally, histograms in the upper right part of the figures show the posterior probability distribution for the observational quantities of interest.

In Figure 4, we report the outcome for the wind properties inspired by the GRMHD simulations of Ciolfi et al. (2017). Here, we are combining together the four different cases APR4q09, APR4q10, H4q09, and H4q10, and we show the outcome of the simulations for our baseline case with $Y_{\rm e} = 0.5$. We found that some of the parameters are well constrained. To begin with, the viewing angle, which was not directly constrained in our procedure, is constrained to $\theta_{\rm l.o.s.} = 23.5^{+5.5}_{-4.5}$ degrees (all quoted uncertainties are at the 1σ statistical significance level, unless stated otherwise), a value that is in good agreement with the estimates based on high-resolution radio imaging (Mooley et al. 2018; Ghirlanda et al. 2019).

Parameters for which we cannot obtain direct limits from observations and which are also well constrained are $\theta_{\rm j}$, η, and $\Delta t_{\rm m-j}$. The injection half-opening angle, never measured for long or short GRBs, is found to be $\theta_{\rm j} = 17.9^{+12.6}_{-3.2}$ degrees. Additionally, we obtained a lower limit for the dimensionless jet entropy (i.e., the maximum attainable Lorentz factor) as $\eta > 240$ at the 3σ level. Finally, we found that the delay time between the merger and the injection of the jet is bound to be rather small: $\Delta t_{\rm m-j} < 0.36$ s. These values are also reported in Table 3, which further shows how such constraints change by considering different electron fractions ($Y_{\rm e} = 1.0$ and 0.2) and stricter constraints on $\Gamma_{\rm l.o.s.}$ and/or the total wind mass $m_{\rm w}$.

For the remaining parameters, our results favor jet energies at the lower edge of the simulated values ($E_{\rm j} \sim 5 \times 10^{48}$ erg), engine activity duration $T_{\rm eng} \sim 2$ s, line-of-sight Lorentz factor $\Gamma_{\rm l.o.s.} \gtrsim 6$, isotropic-equivalent outflow energy along the line of sight $E_{\rm iso,l.o.s.} \sim 2 \times 10^{49}$ erg, and a total mass of the wind in the range $m_{\rm wind} \sim 10^{-3}$–$10^{-2}\ M_\odot$. We note that the finding on the outflow energy is in general agreement with previous constraints from the afterglow modeling.

To check whether our results are sensitive to the different EOS and/or mass ratios under consideration, we show in Figure 5 the two panels $\Delta t_{\rm m-j}$ versus η and $\theta_{\rm l.o.s.}$ versus $\theta_{\rm j}$, corresponding to the most constrained parameters from Figure 4, now separating the four cases. We find that the method is not able to distinguish among the four, with only a marginal difference in the $\theta_{\rm l.o.s.}$ versus $\theta_{\rm j}$ panel for the H4q10 case (rightmost lower panel). This degeneracy reflects the fact that the mass-flow rates and velocities are rather similar despite the different q and EOS.

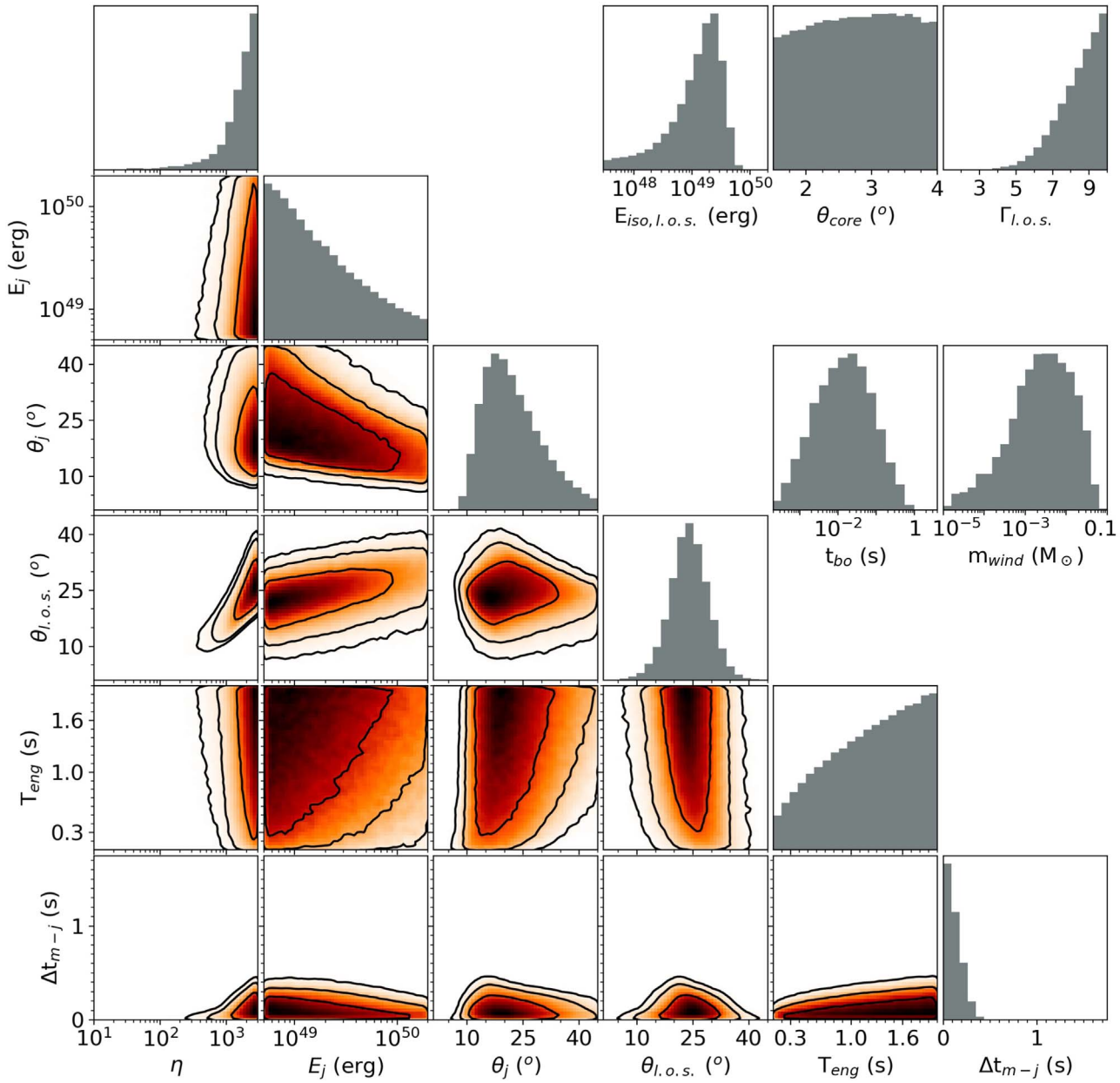

Figure 4. Corner diagram for the six parameters of the model adopting the wind prescriptions inspired by GRMHD simulations by Ciolfi et al. (2017). The results for the four different combinations of EOS and mass ratios are merged together. Solid contour lines show the 1σ, 2σ, and 3σ confidence regions. In addition, probability distributions for the four derived parameters and for the breakout time $t_{\rm bo}$ are shown as histograms in the upper right corner. Note that these show the ratio of the posterior over the prior distributions.

In Figure 6, we select the same two panels from Figure 4, but in this case we show how the result changes by imposing only one of the four observational constraints at a time. The lower limit on η is always reproduced independently from which constraint is imposed, while for the other parameters the outcome is significantly affected by the specific choice. Interestingly, all constraints are consistent with each other at the 1σ level, since the 1σ contours have a non-null intersection.

We now turn to consider the results obtained with a parametrized wind, i.e., allowing for any value of the mass-flow rate and wind velocity within the plausible ranges $0.001 \leqslant \dot{m}_{\rm w}/(M_\odot\ {\rm s}^{-1}) \leqslant 1$ and $0.05 \leqslant v_{\rm w}/c \leqslant 0.25$. The outcome, shown in Figure 7, is qualitatively similar to the previous case (see Figure 4), with the viewing angle and the initial jet half-opening angle well constrained, a lower limit on the jet dimensionless entropy, and an upper limit on the time interval between merger and jet launching.

At a quantitative level, however, some differences emerge. The viewing and jet angles are constrained to different values, namely $\theta_{\rm l.o.s.} = 30.3^{+8.5}_{-8.0}$ degrees and $\theta_{\rm j} = 10.2^{+8.8}_{-3.0}$ degrees, which remain nonetheless consistent within the 1σ range. The constraints on the dimensionless entropy and on the time delay are less stringent: $\eta > 150$ and $\Delta t_{\rm m-j} < 1.1$ s. These variations are brought about by winds that tend to have smaller velocities and smaller total masses compared to the values suggested by the GRMHD simulations of Ciolfi et al. (2017; see Figure 7 and Table 3).

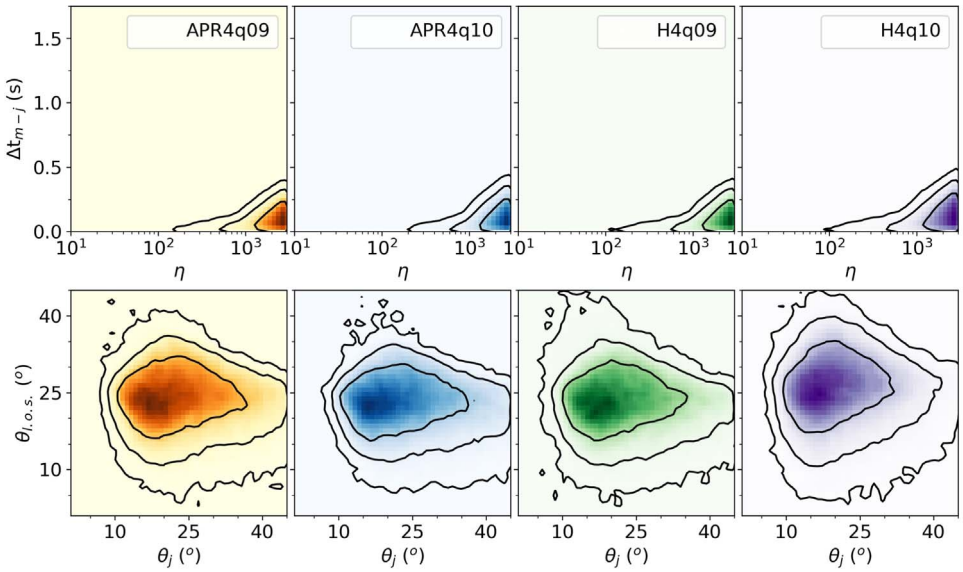

Figure 5. Correlation plots of the two best constrained parameter pairs. The top row shows the $\Delta t_{\rm m-j}$–η plane, while the bottom row shows the $\theta_{\rm l.o.s.}$–$\theta_{\rm j}$ plane. For both parameter pairs, four panels are shown (left to right), corresponding to the four different EOS–mass ratio combinations considered. Solid contour lines show the 1σ, 2σ, and 3σ confidence regions.

Table 3
Results for the Four Most Constrained Parameters: the Merger–Jet Delay, the Asymptotic Lorentz Factor of the Jet, the Viewing Angle, and the Injection Angle

Model	$\Delta t_{\rm m-j}$ (s)	η	$\theta_{\rm l.o.s}$ (°)	$\theta_{\rm j}$ (°)
Simulations; baseline ($Y_e = 0.5$; $\Gamma_{\rm l.o.s.} \leqslant 10$; $m_{\rm w}$ unconstrained)	**<0.36**	**>240**	$\mathbf{23.5^{+5.5}_{-4.5}}$	$\mathbf{17.9^{+12.6}_{-3.2}}$
Simulations; $\Gamma_{\rm l.o.s.} \leqslant 7$	<0.18	>240	$24^{+6.9}_{-3.5}$	$18.4^{+12.5}_{-3.1}$
Simulations; $m_{\rm w} \geqslant 10^{-2}$	<0.37	>390	$23.6^{+4.8}_{-4.5}$	$17.3^{+13.4}_{-2.5}$
Simulations; $\Gamma_{\rm l.o.s.} \leqslant 7$; $m_{\rm w} \geqslant 10^{-2}$	<0.17	>250	$24.1^{+6.7}_{-3.6}$	$19.3^{+11.9}_{-3.9}$
Simulations; $Y_{\rm e} = 1.0$	<0.27	>260	$22.0^{+5.9}_{-}3.3$	$18.1^{+13.4}_{-3.1}$
Simulations; $Y_{\rm e} = 0.2$	<0.51	>170	$25.1^{+5.0}_{-6.0}$	$15.8^{+13.2}_{-1.9}$
Parametric; baseline ($Y_e = 0.5$; $\Gamma_{\rm l.o.s.} \leqslant 10$; $m_{\rm w}$ unconstrained)	**<1.1**	**>150**	$\mathbf{30.3^{+8.5}_{-8.0}}$	$\mathbf{10.2^{+8.8}_{-3.0}}$
Parametric; $\Gamma_{\rm l.o.s.} \leqslant 7$	<0.87	>180	$34.4^{+6.4}_{-8.6}$	$9.2^{+9.7}_{-1.8}$
Parametric; $m_{\rm w} \geqslant 10^{-2}$	<0.87	>420	$27.5^{+6.0}_{-7.1}$	$16.2^{+11.3}_{-3.2}$
Parametric; $\Gamma_{\rm l.o.s.} \leqslant 7$; $m_{\rm w} \geqslant 10^{-2}$	<0.57	>800	$30.7^{+6.2}_{-6.8}$	$16.3^{+13.8}_{-1.2}$
Parametric; $Y_{\rm e} = 1.0$	<1.0	>170	$32.3^{+6.4}_{-9.5}$	$9.6^{+9.0}_{-2.5}$
Parametric; $Y_{\rm e} = 0.2$	<1.2	>130	$30.5^{+8.3}_{-8.8}$	$10.8^{+8.6}_{-3.6}$

Note. Quoted uncertainties are at the 1σ level, while upper and lower limits are 3σ. We highlight in bold the results for our baseline model for both the simulation-inspired wind and the parametric wind cases.

4. Discussion and Conclusions

In this work, we have studied the key properties of the SGRB jet that was launched by the remnant of the BNS merger event GW170817 (Abbott et al. 2017a) and that eventually powered the gamma-ray signal GRB 170817A (Abbott et al. 2017b; Goldstein et al. 2017; Savchenko et al. 2017). We employed the semi-analytic model for the jet–wind interaction developed by Lazzati & Perna (2019) to obtain the properties of the escaping outflow depending on, (i) the properties of the jet at the initial injection from the central engine and (ii) the properties of the massive baryon-loaded wind expelled beforehand by the NS remnant and acting as an obstacle for the propagation of the jet itself. By exploring the plausible parameter ranges with over 100 million random samples and then selecting only cases with an outcome consistent with four main observational constraints (see Section 2), we were able to obtain posterior distributions for the entire parameter set, and hence indications on their most favorable values.

For the wind properties, we assumed an isotropic flow expelled from the time of merger to the time of jet launching with constant mass-flow rate and velocity. In our first analysis, the values of the latter were chosen in accordance to the results of GRMHD BNS merger simulations by Ciolfi et al. (2017), referring to BNSs with two different EOS and two different mass ratios. Then, we considered a more general parametrized wind and explored a wide range of mass-flow rates and velocities.

For the analysis inspired by GRMHD simulations, we found an initial half-opening angle of the jet of $\theta_{\rm j} = 17.9^{+12.6}_{-3.2}$ degrees (at 1σ level) and a robust 3σ lower limit on the dimensionless entropy $\eta = L/\dot{m}c^2 > 240$. We remark that constraints on these intrinsic jet properties are of particular interest, as they cannot be directly obtained from the observations. The rather large lower limit for the injection entropy suggests a low baryon loading, as in the case of electromagnetically driven acceleration mechanisms (Mészáros & Rees 1997; Drenkhahn & Spruit 2002; Metzger et al. 2011).

In addition, we obtained an upper limit on the time delay between the merger and the jet launching: $\Delta t_{\rm m-j} < 0.36$ s at the 3σ level.[10] This limit would imply that most of the

[10] Here we are assuming a fiducial electron fraction of $Y_{\rm e} = 0.5$ within the fireball. For lower values, the photospheric radius would also be reduced, changing the constraint on the time delay $\Delta t_{\rm m-j}$. Even allowing for a quite extreme $Y_{\rm e} = 0.2$, however, the upper limit remains rather small $\Delta t_{\rm m-j} \lesssim 0.51$ s (i.e., about a factor $\sqrt{2.5}$ larger, as expected).

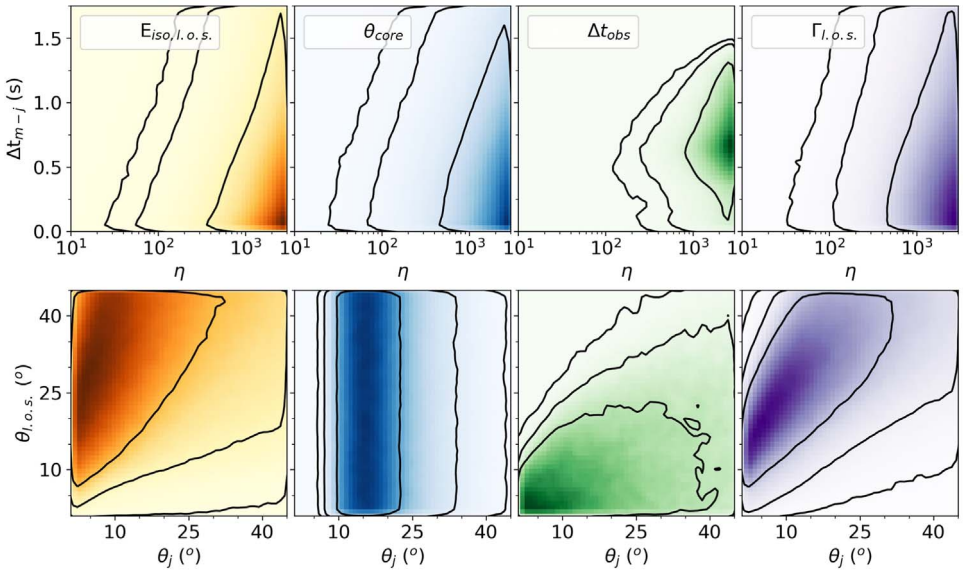

Figure 6. Correlation plots of the two best constrained parameter pairs. The top row shows the $\Delta t_{\rm m-j}$–η plane, while the bottom row shows the $\theta_{\rm l.o.s.}$–$\theta_{\rm j}$ plane. For both parameter pairs, four panels are shown (left to right) with the results obtained by imposing only one observational constrain at a time (see text). Solid contour lines show the 1σ, 2σ, and 3σ confidence regions.

observed delay ($\approx$1.74 s) is due to the outflow breaking out of the wind and its subsequent propagation until the photospheric radius is reached (along the line of sight), in agreement with the idea that the similarity between the gamma-ray pulse duration and the total observed delay is not a simple coincidence (Lin et al. 2018; Zhang et al. 2018). This is also in agreement with populations studies on SGRBs (Beniamini et al. 2020a). Such a result is likely influenced by the fairly large prompt emission energetics and, at the same time, by the fact that the Lorentz factor of the emerging outflow along the line of sight could not be too large to account for the late onset of the afterglow emission (Hallinan et al. 2017; Troja et al. 2017). These two features, when taken together, imply that the fireball carried a significant number of baryons, therefore pushing the photosphere to relatively large radii. We note that the change from a jet released with high η value to an outflow with a significant rest-mass component requires baryon loading during the interaction of the jet with the wind material. Since the photosphere location is of such importance for estimating the propagation delay, we have derived in this paper a formula for the photospheric radius that relaxes the two commonly used approximations of either an infinite wind or a thin shell (see Equation (6)).

The above upper limit $\Delta t_{\rm m-j} \lesssim 0.4$ s has potentially important implications. In particular, under the assumption that the central engine launching the jet was a newly-formed BH, as currently favored by GRMHD BNS merger simulations (Ruiz et al. 2016; Ciolfi 2020a; see Ciolfi (2020b) for a recent review), this constraint would imply a NS remnant lifetime $\lesssim$0.4 s. In turn, this would help in further constraining the NS EOS, as well as physical models of the kilonova that accompanied the 2017 August event.

By looking at the other parameters, we note that the total jet energy and the engine duration are found in general agreement with the observations (see, e.g., Ghirlanda et al. 2019 and Abbott et al. 2017b, respectively), while the indication on the Lorentz factor along the line of sight, $\Gamma_{\rm l.o.s.} \gtrsim 6$, is at the higher end of (but still consistent with) the range of available estimates, for which $\Gamma_{\rm l.o.s.}$ should not be larger than $\approx$7 (e.g., Beniamini et al. 2020b). The viewing angle is constrained rather well and is also consistent (within the 1σ range) with the latest radio observations (Mooley et al. 2018; Ghirlanda et al. 2019). Finally, the favored range for the total mass in the wind is $m_{\rm wind} \sim 10^{-3}$–$10^{-2}\,M_\odot$. We note that this is only marginally consistent with a scenario in which (i) the jet was launched after the collapse to a BH (Ciolfi 2020a) and (ii) the wind from the NS remnant is what mainly powered the early "blue" component of the associated kilonova (as assumed, e.g., in Gill et al. 2019); indeed, such a scenario would require a mass as high as $\sim 10^{-2}\,M_\odot$ for the unbound portion of the wind material (e.g., Villar et al. 2017).

For completeness, we also checked how the constraints change by imposing $\Gamma_{\rm l.o.s.} \leqslant 7$ (as in Beniamini et al. 2020b) and/or $m_{\rm wind} \geqslant 10^{-2}\,M_\odot$ (to better accommodate the hypothesis of the blue kilonova being powered by the NS remnant wind and the jet being launched after the collapse to a BH). The additional condition on $\Gamma_{\rm l.o.s.}$ has the interesting effect of further reducing the upper limit on $\Delta t_{\rm m-j}$ by a factor around 2, while the other results are poorly affected. The additional condition on $m_{\rm wind}$ does not show a significant effect on $\Delta t_{\rm m-j}$, but makes the lower limit on η more stringent (although this effect disappears when both the additional conditions are applied).

The analysis based on a parametrized wind confirmed the above overall picture, although with some quantitative differences. Not surprisingly, we found that the derived constraints are relaxed once we allow for a broader range of mass-flow rates and wind velocities, especially if we consider a very low electron fraction. The merger–jet time delay, in particular, is constrained to $\Delta t_{\rm m-j} < 1.1$ s (at 3σ), which is less restrictive. We also note that in this case small wind velocities (lower than 0.1 c) appear to be favored, as well as total wind masses no larger than few $\times\ 10^{-3}\,M_\odot$. Finally, this analysis favors a viewing angle of $\theta_{\rm l.o.s.} = 30.3^{+8.5}_{-8.0}$ degrees that is somewhat larger than that estimated from high-resolution radio imaging (Mooley et al. 2018; Ghirlanda et al. 2019), causing

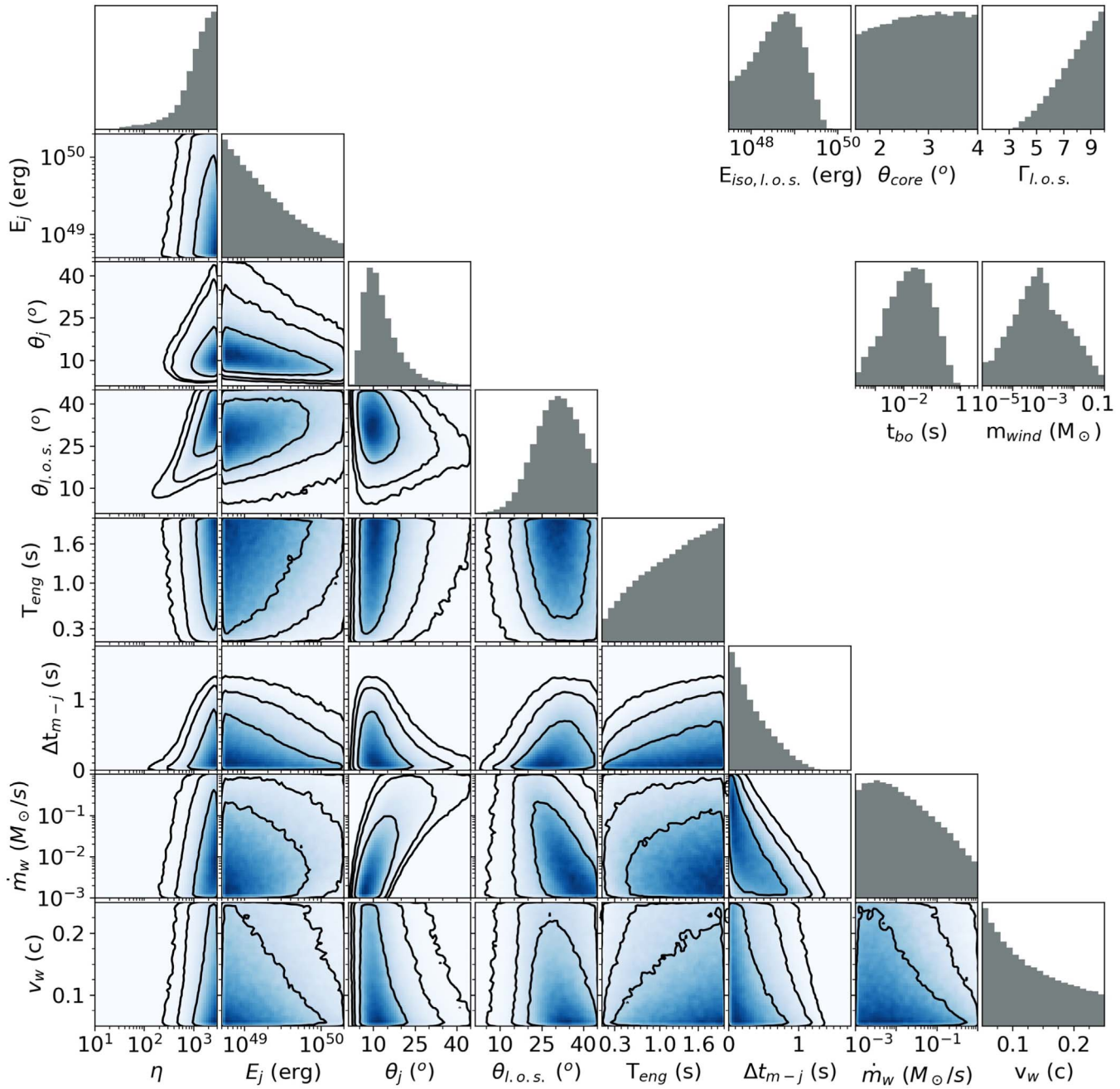

Figure 7. Analogous to Figure 4 but for the case of a parametrized wind. In this case, the model has two additional parameters, i.e., the mass-flow rate and the velocity of the wind.

some strain with the observations. In this case, the additional conditions on $\Gamma_{\rm l.o.s.}$ and $m_{\rm wind}$ lower significantly the upper limit on $\Delta t_{\rm m-j}$, substantially enlarge the lower limit on η, and also increase $\theta_{\rm j}$ up to values similar to the simulation-inspired wind case.

As a general note of caution, we remark that in this work we assumed constant mass-flow rates and velocities for the baryon-loaded wind produced by the NS remnant. This simplifying assumption may have relevant effects on the outcome of our analysis. Relaxing this assumption and employing time-evolving wind properties (possibly motivated by BNS merger simulation results) will be the subject of future investigation.

While our approach can be further refined, the present study shows its potential. In particular, the possibility of inferring the intrinsic jet properties at the time the jet itself is launched by the central engine can provide a valuable input for the investigation of jet launching mechanisms via numerical simulations. We also stress that here we applied the model to the case of GW170817/GRB 170817A, but our method is general and can be readily applied to any other SGRB observed in the future.

D.L. acknowledges support from NASA grants 80NSSC 18K1729 (Fermi) and NNX17AK42G (ATP), Chandra grant

TM9-20002X, and NSF grant AST-1907955. R.P. acknowledges support by NSF award AST-1616157.

ORCID iDs

Davide Lazzati https://orcid.org/0000-0002-9190-662X
Riccardo Ciolfi https://orcid.org/0000-0003-3140-8933
Rosalba Perna https://orcid.org/0000-0002-3635-5677

References

Abbott, B. P., Abbott, R., Abbott, T. D., et al. 2017a, PhRvL, 119, 161101
Abbott, B. P., Abbott, R., Abbott, T. D., et al. 2017b, ApJL, 848, L13
Abbott, B. P., Abbott, R., Abbott, T. D., et al. 2017c, ApJL, 848, L12
Akmal, A., Pandharipande, V. R., & Ravenhall, D. G. 1998, PhRvC, 58, 1804
Alexander, K. D., Margutti, R., Blanchard, P. K., et al. 2018, ApJL, 863, L18
Arcavi, I., Hosseinzadeh, G., Howell, D. A., et al. 2017, Natur, 551, 64
Begelman, M. C., & Cioffi, D. F. 1989, ApJL, 345, L21
Belczynski, K., Perna, R., Bulik, T., et al. 2006, ApJ, 648, 1110
Beloborodov, A. M. 2003, ApJ, 588, 931
Beniamini, P., Barniol Duran, R., Petropoulou, M., & Giannios, D. 2020a, ApJ, 895, 33
Beniamini, P., Granot, J., & Gill, R. 2020b, MNRAS, 493, 3521
Bromberg, O., Nakar, E., Piran, T., & Sari, R. 2011, ApJ, 740, 100
Ciolfi, R. 2018, IJMPD, 27, 1842004
Ciolfi, R. 2020a, MNRAS, 495, L66
Ciolfi, R. 2020b, GReGr, 52, 59
Ciolfi, R., Kastaun, W., Giacomazzo, B., et al. 2017, PhRvD, 95, 063016
Ciolfi, R., Kastaun, W., Kalinani, J. V., & Giacomazzo, B. 2019, Phys. Rev. D, 100, 023005
Daigne, F., & Mochkovitch, R. 2002, MNRAS, 336, 1271
D'Avanzo, P., Campana, S., Salafia, O. S., et al. 2018, A&A, 613, L1
Drenkhahn, G., & Spruit, H. C. 2002, A&A, 391, 1141
Fernández, R., & Metzger, B. D. 2013, MNRAS, 435, 502
Fong, W., Berger, E., Margutti, R., & Zauderer, B. A. 2015, ApJ, 815, 102
Ghirlanda, G., Salafia, O. S., Paragi, Z., et al. 2019, Sci, 363, 968
Gill, R., Nathanail, A., & Rezzolla, L. 2019, ApJ, 876, 139
Glendenning, N. K., & Moszkowski, S. A. 1991, PhRvL, 67, 2414
Goldstein, A., Veres, P., Burns, E., et al. 2017, ApJL, 848, L14
Granot, J., Guetta, D., & Gill, R. 2017, ApJL, 850, L24
Hallinan, G., Corsi, A., Mooley, K. P., et al. 2017, Sci, 358, 1579
Hamidani, H., Kiuchi, K., & Ioka, K. 2020, MNRAS, 491, 3192
Hotokezaka, K., Nakar, E., Gottlieb, O., et al. 2019, NatAs, 3, 940
Ioka, K., & Nakamura, T. 2018, PTEP, 2018, 043E02
Kasliwal, M. M., Nakar, E., Singer, L. P., et al. 2017, Sci, 358, 1559
Kouveliotou, C., Meegan, C. A., Fishman, G. J., et al. 1993, ApJL, 413, L101
Lamb, G. P., Lyman, J. D., Levan, A. J., et al. 2019, ApJL, 870, L15
Lamb, G. P., Mandel, I., & Resmi, L. 2018, MNRAS, 481, 2581
Lazzati, D., & Begelman, M. C. 2005, ApJ, 629, 903
Lazzati, D., Deich, A., Morsony, B. J., & Workman, J. C. 2017a, MNRAS, 471, 1652
Lazzati, D., López-Cámara, D., Cantiello, M., et al. 2017b, ApJL, 848, L6
Lazzati, D., & Perna, R. 2019, ApJ, 881, 89
Lazzati, D., Perna, R., Morsony, B. J., et al. 2018, PhRvL, 120, 241103
Lin, D.-B., Liu, T., Lin, J., et al. 2018, ApJ, 856, 90
Lyman, J. D., Lamb, G. P., Levan, A. J., et al. 2018, NatAs, 2, 751
Lyutikov, M. 2020, MNRAS, 491, 483
MacFadyen, A. I., Woosley, S. E., & Heger, A. 2001, ApJ, 550, 410
Matzner, C. D. 2003, MNRAS, 345, 575
Mészáros, P., & Rees, M. J. 1997, ApJL, 482, L29
Mészáros, P., & Rees, M. J. 2000, ApJ, 530, 292
Metzger, B. D., Giannios, D., Thompson, T. A., Bucciantini, N., & Quataert, E. 2011, MNRAS, 413, 2031
Mooley, K. P., Deller, A. T., Gottlieb, O., et al. 2018, Natur, 561, 355
Morsony, B. J., Lazzati, D., & Begelman, M. C. 2007, ApJ, 665, 569
Murguia-Berthier, A., Montes, G., Ramirez-Ruiz, E., De Colle, F., & Lee, W. H. 2014, ApJL, 788, L8
Murguia-Berthier, A., Ramirez-Ruiz, E., Montes, G., et al. 2017, ApJL, 835, L34
Nagakura, H., Hotokezaka, K., Sekiguchi, Y., Shibata, M., & Ioka, K. 2014, ApJL, 784, L28
Nakar, E., Gottlieb, O., Piran, T., Kasliwal, M. M., & Hallinan, G. 2018, ApJ, 867, 18
Nakar, E., & Piran, T. 2018, MNRAS, 478, 407
Pian, E., D'Avanzo, P., Benetti, S., et al. 2017, Natur, 551, 67
Radice, D., Perego, A., Hotokezaka, K., et al. 2018, ApJL, 869, L35
Rosswog, S., Liebendörfer, M., Thielemann, F.-K., et al. 1999, A&A, 341, 499
Ruiz, M., Lang, R. N., Paschalidis, V., & Shapiro, S. L. 2016, ApJL, 824, L6
Salafia, O. S., Barbieri, C., Ascenzi, S., & Toffano, M. 2020, A&A, 636, 105
Savchenko, V., Ferrigno, C., Kuulkers, E., et al. 2017, ApJL, 848, L15
Soares-Santos, M., Holz, D. E., Annis, J., et al. 2017, ApJ, 848, L16
Troja, E., Piro, L., van Eerten, H., et al. 2017, Natur, 551, 71
Villar, V. A., Guillochon, J., Berger, E., et al. 2017, ApJL, 851, L21
Wu, Y., & MacFadyen, A. 2018, ApJ, 869, 55
Xie, X., Zrake, J., & MacFadyen, A. 2018, ApJ, 863, 58
Zhang, B. 2019, FrPhy, 14, 64402
Zhang, B. B., Zhang, B., Sun, H., et al. 2018, NatCo, 9, 447